energies

MDPI

Article

Improvement of Transient Stability in a Hybrid Power Multi-System Using a Designed NIDC (Novel Intelligent Damping Controller)

Ting-Chia Ou [1], Kai-Hung Lu [2,*] and Chiou-Jye Huang [2]

[1] Institute of Nuclear Energy Research, Taoyuan 32546, Taiwan; tcou@iner.gov.tw
[2] School of Information Technology, Beijing Institute of Technology, Zhuhai 519088, China; chioujye@itri.org.tw
* Correspondence: khluphd@gmail.com; Tel.: +86-137-2624-7655

Academic Editor: William Holderbaum
Received: 8 November 2016; Accepted: 31 March 2017; Published: 5 April 2017

Abstract: This paper endeavors to apply a novel intelligent damping controller (NIDC) for the static synchronous compensator (STATCOM) to reduce the power fluctuations, voltage support and damping in a hybrid power multi-system. In this paper, we discuss the integration of an offshore wind farm (OWF) and a seashore wave power farm (SWPF) via a high-voltage, alternating current (HVAC) electric power transmission line that connects the STATCOM and the 12-bus hybrid power multi-system. The hybrid multi-system consists of a battery energy storage system (BESS) and a micro-turbine generation (MTG). The proposed NIDC consists of a designed proportional–integral–derivative (PID) linear controller, an adaptive critic network and a proposed functional link-based novel recurrent fuzzy neural network (FLNRFNN). Test results show that the proposed controller can achieve better damping characteristics and effectively stabilize the network under unstable conditions.

Keywords: static synchronous compensator (STATCOM); offshore wind farm (OWF); seashore wave power farm (SWPF); functional link-based novel recurrent fuzzy neural network (FLNRFNN); novel intelligent damping controller (NIDC)

1. Introduction

Wind energy and ocean wave energy are gaining interest as renewable and clean power sources. Various control strategies have been proposed to achieve the desired speed control on wind generators and seashore wave energy systems [1,2]. In recent years, both offshore wind farms (OWFs) and seashore wave power farms (SWPFs) have been evaluated and are now in commercial operation [2]. Combined OWFs and SWPFs are evaluated and developed in the seas around Western Europe and the United Kingdom [3].

When OWFs and SWPFs deliver or trip a large amount of electric power via the grid simultaneously, the inherent power fluctuations that occur can have adverse impacts on the power quality of the systems to which they are connected. In recent years, the battery energy storage system (BESS) has become more important than ever before because of the growing penetration of intermittent renewable energy sources [4–6]. When the BESS is connected to power grid, the BESS should adjust the whole power flow direction according to the renewable energy and load specific to the power multi-system. This paper thus proposes the use of a static synchronous compensator (STATCOM) in order to reduce the power fluctuations, voltage support and damping, and thus improves the transient stability of a 12-bus hybrid power multi-system connected for the integration of wind farms and wave

power farms. The multi-system consists of a BESS, a synchronous generator (SG) and a micro turbine generator (MTG).

In recent years, Smart grids and microgrids are becoming important topics for energy demand. The microgrid paves a way to effectively integrate various sources of distributed generation (DG), especially renewable energy sources, and thus reduce CO_2 emissions. However, it must be considered that increasing levels of penetration of DGs may cause severe phase voltage imbalance, resulting in a larger ground current and descending power quality. A systematic study with an effective solution approach is crucial to maintain a good quality of supplying power, thereby motivating the study made in this paper. Much of the literature proposed control methods for the STATCOM to improve the damping of power oscillations, such as the use of state feedback control techniques or other linear damping controllers [7–10]. Some studies have proposed external controllers using intelligent control schemes, such as fuzzy logic controllers, neuro-fuzzy external controllers, hybrid controllers and a Gray-Based Genetic algorithm method [11–13]. However, the literature showing improved results is very limiting. In this paper, the functional link-based novel recurrent fuzzy neural network (FLNRFNN) is a novel fuzzy neural network structure, which uses a functional-link neural network to generate a set of linearly independent functions, and functionally expands the elements of the input variables. Accordingly, it can be computed more quickly and also provides favorable performance results when the outer product term is taken into account in the function expansion. For the training sensitivity, the adaptive critic network is applied in this paper in order to provide suitable training signals for the FLNRFNN.

With the dynamics being continually identified by a model, the recurrent fuzzy neural networks (RFNN) are suitable for multivariable applications, especially for a system with unclear and complex dynamics [13,14]. This paper used the functional-link neural network (FLNN) to strengthen the performance of the novel RFNN (NRFNN). The input variables are trigonometric basis functions and the linearly independency is used for a functional expansion of the FLNN in the extended space for classification. Moreover, FLNN can capture nonlinear input–output relationships effectively by the suitable set of polynomial inputs, since the high-order effects are incorporated in the input variables into higher dimensions of the input space [15–17].

This paper proposed a novel intelligent damping controller (NIDC) for the STATCOM to damp power system oscillations. The proposed NIDC consists of a proposed designed PID linear controller based on a theory of modal control, the adaptive critic network and the proposed FLNRFNN. The NIDC for the STATCOM is developed to improve both transient stability and system oscillations. The performance of conventional controllers degrades under such an environment, and needs to be returned to keep the desired performance a weakness the FLNRFNN approach can overcome. The designed PID linear controller is an analysis of the eigenvalues and root locus in the complex plane. A linearized model using eigenvalue analysis subject to the power fluctuations is performed to verify the effectiveness of the designed PID controller.

The adaptive critic network is evaluated in relation to the FLNRFNN controller, so the output signal can be provided the corrections of the designed PID to achieve the optimal damping control signal for STATCOM. The NIDC is unlike conventional controllers, the performances of which degrade for such changes and require retuning to produce the desired performance. The major contribution of this paper is discovering that a robust NIDC joined to the STATCOM can mitigate the power oscillations effectively in a hybrid power multi-system which connects the integration of a OWF and a SWPF.

2. Analysis of System Models

Figure 1 shows the system examined in this paper. The system contains 200 MW doubly-fed induction generator (DFIG)-based OWF, 120 MW squirrel cage induction generator (SCIG)-based SWPF, BESS (128 MW, 11.4 kV), MTG (192 MVA, 11.4 kV) and 134 MVA STATCOM. The OWF is

expressed by wind turbines and the SWPF is expressed by Wells turbines, which are connected to bus 4 through a 33 kV high-voltage, alternating current (HVAC) electric power transmission line.

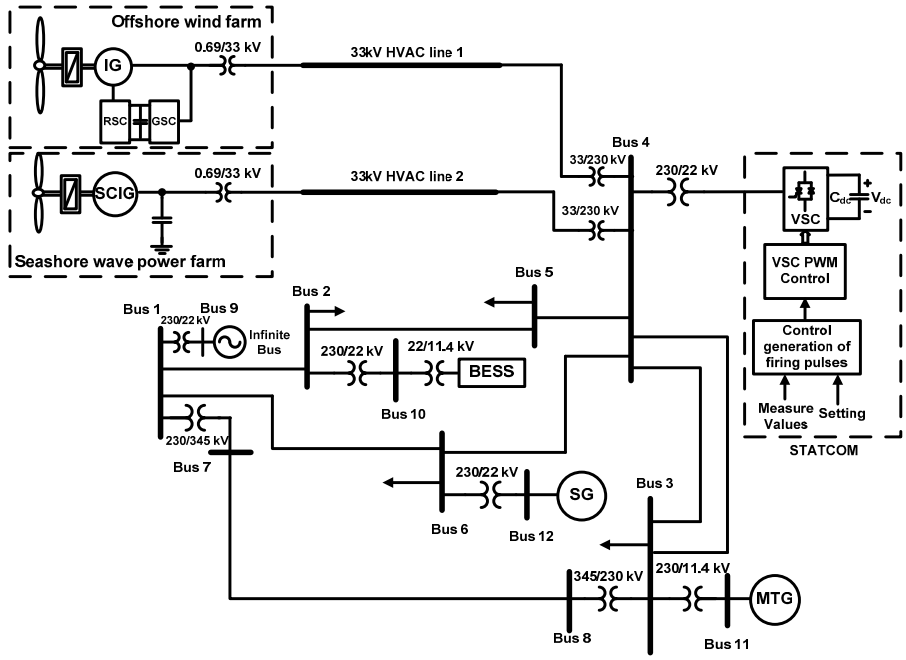

Figure 1. The 12-bus hybrid power multi-system connecting the integration of offshore wind farms and seashore wave power farms with the STATCOM.

2.1. Wind Turbine Characteristics

The wind turbine input is the variable wind and the output is the mechanical power turning the generator rotor blades [10]. The output mechanical power available from a wind turbine can be obtained by:

$$P_m = 0.5\rho \cdot V_\omega^3 \cdot A \cdot C_p(\lambda, \beta) \tag{1}$$

where the tip speed ratio $\lambda = \omega_r r / V_\omega$. C_p is a function of the λ, and is generally defined with [13]:

$$C_p = C_{p1}\left(\frac{C_{p2}}{\lambda_i} - C_{p3}\cdot\beta - C_{p4}\cdot\beta^{C_{p5}} - C_{p6}\right)e^{\frac{-C_{p7}}{\lambda_i}} \tag{2}$$

$$\lambda_i = \frac{1}{\frac{1}{\lambda - C_{p8}\beta} - \frac{C_{p9}}{\beta^3+1}} \tag{3}$$

where C_{p1} to C_{p9} are the wind turbine constant coefficients of C_p.

2.2. DFIG

The wind generator chosen for this study is a three-phase DFIG, shown in Figure 1. The DFIG consists of the turbine, rotor side converter (RSC) and grid side converter (GSC) via a dc link. The detail configuration and control models of DFIG system in the *d-q* common reference frame are referred to in [18]. T_m, T_e and torque equation can be expressed as:

$$T_m = \frac{P_m}{\omega_r} \tag{4}$$

$$T_e = \frac{P_e}{\omega_e} = \frac{2}{n_p}\frac{P_e}{\omega_r} \tag{5}$$

$$J\frac{d\omega_r}{dt} = T_m - B\omega_r - T_e \tag{6}$$

2.3. Wells Turbine

The Wells turbine drives an SCIG mounted on the same shaft and the captured mechanical torque (T_s) from the seashore wave can be found from [2]:

$$T_s = KC_T\left(V^2 + (r+\omega)^2\right) \tag{7}$$

$$C_T = \frac{C_{T1}\delta^3 - C_{T2}\delta^2 + C_{T3}\delta - C_{T4}}{C_{T5}\delta^2 + C_{T6}\delta - C_{T7}} + C_{T8} \tag{8}$$

$$\delta = \angle\tan^{-1}\left(\frac{r+\omega}{V}\right) \tag{9}$$

where r and ω are the turbine radius and shaft angular speed, respectively. C_{T1}–C_{T8} are the Wells turbine torque constant coefficients of C_T.

2.4. BESS and MTG

The BESS serves as an independent voltage source for supplying power to the multi-system. A sensitivity matrix is used to calculate the injection current needed to keep the BESS's internal voltage constant. The relationships of voltage variations can be expressed as [4]:

$$[\mathrm{V_B}] - [\mathrm{V_{BESS}}] = [\mathrm{Z_B}][\mathrm{I_{BESS}}] \tag{10}$$

2.5. MTG

The MTG system is widely used for power generation applications. The micro turbine can augment utility supply during peak load periods, thus increasing power reliability and reducing or eliminating peak demand charges. The model of the MTG unit consists of a micro turbine, permanent magnet synchronous machine, machine and grid side converters with control and filter. It operates on the speed error formed between a reference speed and the rotor speed of the MTG. It is the radical means of control for the micro turbine under different load conditions. More mathematical equations of the turbine torque and fuel mass flow rate and air mass flow rates, thermal and detail control block diagram of converters for an MTG can be found in [19,20].

2.6. STATCOM

The STATCOM can supply both the capacitive and the inductive compensation to support the bus voltage (V_S) by independently controlling its output current. The real current is responsible for controlling the real power, while the active current is used to control the reactive power and exchange it between the STATCOM and the power system. It is also capable of improving the power system stability. The STATCOM is controlled by the external damping controller to damp the reference signal of the dc voltage [8]. The control block of the traditions external damping controller of the STATCOM is shown in Figure 2 (the SW_1 is closed and SW_2 is opened).

V_S* and V_{dc}* are reference signals for the bus voltage and dc link voltage of the STATCOM. K_{p1}, K_{p2}, K_{i1}, and K_{i2} are the proportional and integral gains for PI controllers, respectively. V_{shq0} and V_{shd0} are the initial values for the d-q axis voltages under a synchronous reference frame. The direct and quadrature components of the voltages are then used to generate the m and α, which are then provided to the Pulse Width Modulation (PWM) generator which generates the gating signals for the power electronic switches in Voltage Source Converter (VSC). The d-q axis voltages V_{shd} and V_{shq} can be expressed as:

$$V_{shd} = m \cdot V_{dc} \cdot \sin(\delta_s + \alpha) \tag{11}$$

$$V_{shq} = m \cdot V_{dc} \cdot \cos(\delta_s + \alpha) \tag{12}$$

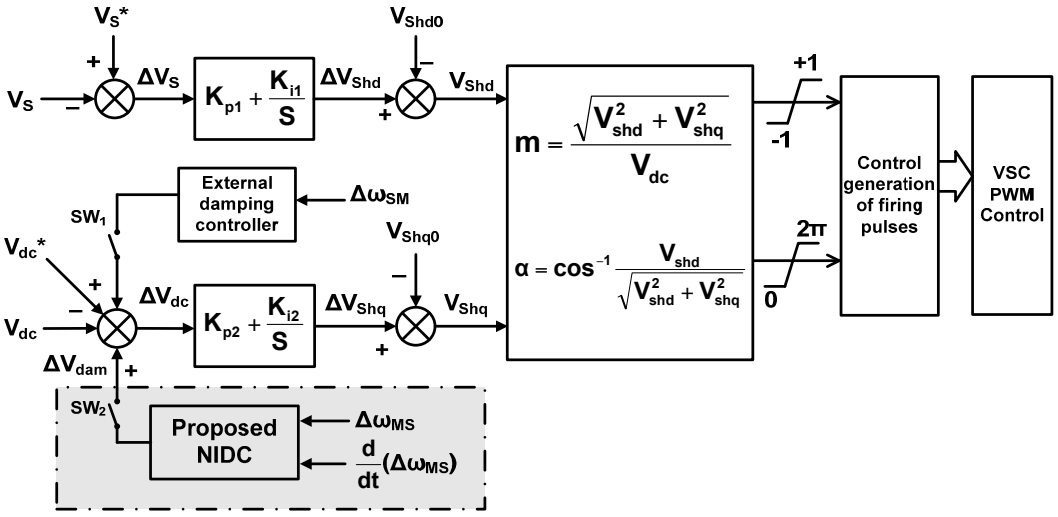

Figure 2. The control block of the STATCOM with damping controller.

The dc link of the STATCOM equation can be expressed as:

$$\frac{dV_{dc}}{dt} = \frac{-1}{C_{dc}}\left(I_{dc} + \frac{V_{dc}}{R_p}\right) \tag{13}$$

$$I_{dc} = m\left[i_{dcd} sin(\delta_s + \alpha) + i_{dcq} cos(\delta_s + \alpha)\right] \tag{14}$$

The proposed NIDC for the STATCOM shown in Figure 3 (the SW_1 is opened and SW_2 is closed in Figure 2, and SW_3 of Figure 3 is closed) can improve the dynamic stability of the hybrid power multi-system. It consists of the critic network, FLNRFNN and a PID controller. Because the generator speed deviations are easier to obtain in practice by measurement and analysis, the inputs of the damping loops are the generator speed deviation between the MTG and SG ($\Delta\omega_{MS}$) in relation to the NIDC. The main function of the STATCOM is to regulate the line voltage at the point of connection, which can be used to mitigate the power oscillations. However, in the various operating conditions of the power system, the performance of the linear external controller will be significantly affected by changes in wind speed, especially if the transient state occurred.

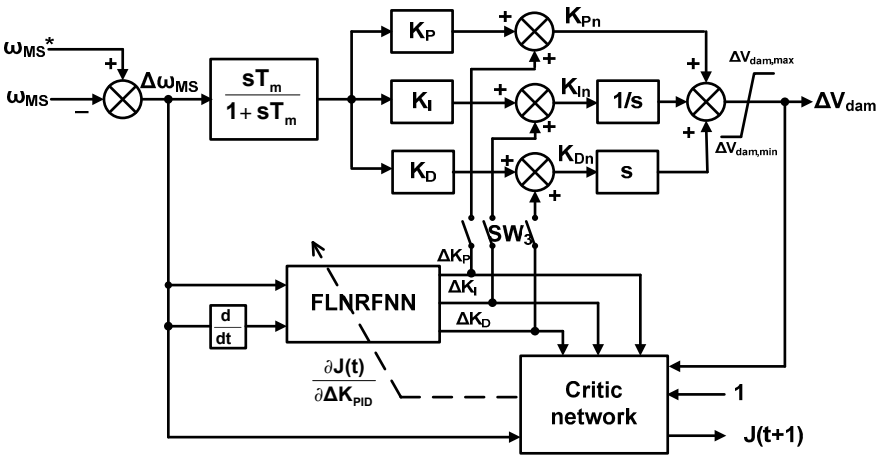

Figure 3. Proposed NIDC for the STATCOM.

3. Design an NIDC for the STATCOM

The damping controller input signal should be the rotor speed deviation between the MTG and SG ($\Delta\omega_{\mathrm{MS}}$). The proposed NIDC consists of three parts: the adaptive critic network, the FLNRFNN, and a PID controller, as shown in Figure 3. An FLNRFNN is adopted to implement the function expansion for the FL (Functional Link)-based NRFNN, to improve the accuracy of the function approximation. The adaptive critic network is applied in order to provide suitable training signals for the FLNRFNN controller. The FLNRFNN produces the variation gains values ΔK_{PID} (ΔK_P, ΔK_I and ΔK_D) of the PID controller. Therefore, the proposed NIDC is added to the voltage reference V_{dc}* of the STATCOM and it is capable of providing near optimal results for complex and hybrid power multi-system connected the integration of the OWF and SWPF systems in order to mitigate the power oscillations and to improve stability.

3.1. PID Damping Controller

The PID damping controller is an analysis of complex eigenvalues based on a theory of modal control. The matrix of state space and the transfer function are as follows [10]:

$$\dot{\mathbf{X}} = \mathbf{AX} + \mathbf{BR} \tag{15}$$

$$\mathbf{Y = CX + DR} \tag{16}$$

$$\mathbf{T(s)} = \mathbf{Y(s)/R(s)} \tag{17}$$

where $\mathbf{X}$ and $\dot{\mathbf{X}}$ are the state variables matrix and its differential operator; $\mathbf{R}$ is the plant input matrix $\Delta\omega_{\mathrm{MS}}$. $\mathbf{Y}$ corresponds to the system output ΔV_{dam}, as shown in Figure 3. $\mathbf{A}$, $\mathbf{B}$, $\mathbf{C}$ and $\mathbf{D}$ are the constants of suitable system dimensions matrices. The state vectors of $\mathbf{X} = [\mathbf{X_{OWF}}, \mathbf{X_{SWPF}}, \mathbf{X_{tur}}, \mathbf{X_{STATCOM}}, \mathbf{X_{AC}}]^{\mathrm{T}}$, where $\mathbf{X_{AC}}$ is the state vector of the hybrid multi-machine system, including the SG, BESS, MTG, transmission lines and buses system.

The transfer function $T(s)$ is represented as [10]:

$$T(s) = \Delta\alpha_{dam}/\Delta V_S = sT_m/1 + sT_m(K_P + K_I/s + sK_D) \tag{18}$$

where K_P, K_I and K_D are the gains for the PID controller.

The stable and unstable state of the hybrid system with/without the OWF, SWPF and the STATCOM with/without PID controller can be found by complex eigenvalues λ_1–λ_{21} as shown in Table 1 under 12 m/s and 8 m/s for the OWF and SWPF. The λ_1–λ_9 refer to the modes of hybrid multi-machine system. The λ_{10}–λ_{15} refer to the electric modes of the OWF and SWPF. The λ_{16}–λ_{18} are the modes of wind and Wells turbines. The λ_{19}–λ_{21} are the modes of the STATCOM. Most of the eigenvalues are fixed on the left side of the imaginary axis. The two sets of eigenvalues λ_3 and λ_5 are close to the imaginary axis. Hence, from the column with the PID term of Table 1, the λ_3 and λ_5 of the STATCOM with the PID controller have been prespecified and positioned in the appropriate place on the complex plane. From the column, all eigenvalues are seen to be stable. The λ_3 and λ_5 are substituted to a characteristic equation. The suitable values of $K_P = -15.21$, $K_I = -16.89$, $K_D = 10.01$ and $T_m = 0.58$ can be determined. From the analysis of root locus, Figure 4a,b compares the results of root locus for the eigenvalues of rotor angle of MTG δ_{M} and SG δ_{S} under the OWF from 4 to 20 m/s and the SWPF at 8 m/s. It can be clearly seen that the STATCOM with the designed PID can keep stable operation and move more to the left of the imaginary axis.

Table 1. The analysis of eigenvalues.

Eigenvalues	Hybrid System without OWF, SWPF and STATCOM	Hybrid System with OWF, SWPF and STATCOM without PID	Hybrid System with OWF, SWPF and STATCOM with Designed PID
λ_1	$-0.918 \pm$ j18.788	$-1.122 \pm$ j19.683	$-1.122 \pm$ j19.683
λ_2	-28.794, -5.426	-31.526, -6.632	-31.531, -5.766
λ_3	$-0.180 \pm$ j9.366	$-0.193 \pm$ j10.407	$-0.651 \pm$ j9.90
λ_4	$-5.454 \pm$ j8.244	$-5.713 \pm$ j8.637	$-5.945 \pm$ j8.512
λ_5	$-0.178 \pm$ j7.017	$-0.186 \pm$ j7.351	$-0.550 \pm$ j7.810
λ_6	$-0.467 \pm$ j0.022	$-0.490 \pm$ j0.071	$-0.437 \pm$ j0.682
λ_7	$-0.416 \pm$ j0.634	$-0.436 \pm$ j0.6054	$-0.393 \pm$ j0.321
λ_8	$-0.395 \pm$ j0.416	$-0.414 \pm$ j0.435	$-0.601 \pm$ j0.834
λ_9	-4.192, -3.387	-4.392, -3.548	-31.531, -5.766
λ_{10}		$-0.806 \pm$ j9895.182	$-0.806 \pm$ j9895.182
λ_{11}		$-47.9644 \pm$ j1203.51	$-47.9644 \pm$ j1203.51
λ_{12}		-108.48, -100	-108.48, -100
λ_{13}		$-25.6377 \pm$ j408.012	$-25.6377 \pm$ j408.012
λ_{14}		$-16.7684 \pm$ j412.742	$-16.7684 \pm$ j412.742
λ_{16}		-1.184, -0.309	-1.184, -1.781
λ_{17}		-109.710, -110.132	110.022, -109.343
λ_{18}		$-0.344 \pm$ j0.596	$-0.3641 \pm$ j0.202
λ_{19}		-0.281	-0.281
λ_{20}		$-2.354 \pm$ j3.74	$-2.354 \pm$ j3.74
λ_{21}		$-2.024 \pm$ j1.023	$-2.001 \pm$ j1.109

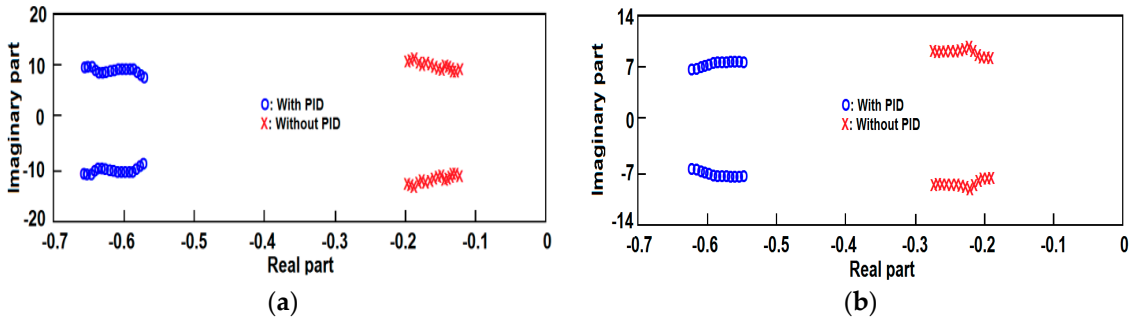

Figure 4. The results of root locus for the eigenvalues (**a**) the rotor angle δ_S; (**b**) the rotor angle δ_M.

3.2. FLNFRNN

Figure 5 shows the design of the FLNRFNN. It has an input layer, a current membership layer with a Gaussian function, a recurrent fuzzy rule layer, a FLNN layer, and an output layer that is connected with an FLNN. The Membership layer and fuzzy rule layer are fed back to themselves through a time delay z^{-1}. There are two input variables, 10 membership nodes, 25 fuzzy rule nodes and two output nodes in this paper, where the number of nodes can be adjusted according to the knowledge of various applications. The FLNN uses a feed forward neural network structure to generate a set of linearly independent functions, and functionally expands the elements of the input variables. The trigonometric function is used in the FLNN, since it can be computed more quickly than the Gaussian, the sine and the cosine functions. Moreover, it also provides better performance when the outer product term is taken into account in the function expansion [15,17]. The input vector $\boldsymbol{X} = [X_1, X_2]^T$ is a functional expansion that uses a trigonometric polynomial basis function, and can be written in the enhanced space as $\boldsymbol{\psi} = [\psi_1, \psi_2, \ldots, \psi_p] = [1, X_1, \sin(\pi X_1), \cos(\pi X_1), X_1X_2, \sin(\pi X_2), \cos(\pi X_2), X_1X_2]$, where X_1X_2 is the outer product term. Furthermore, the FLNN output is expressed by a linear sum of the yth node as:

$$\hat{f}_y(k) = \theta\left(\sum_E \psi_E(x_i)\cdot w_{Ey}\right) = \theta\left(w_{Ey}\cdot\psi_E(\boldsymbol{X})\right),\ E = 1, 2, \ldots, 9 \text{ and } y = 1, 2, \ldots, 9 \tag{19}$$

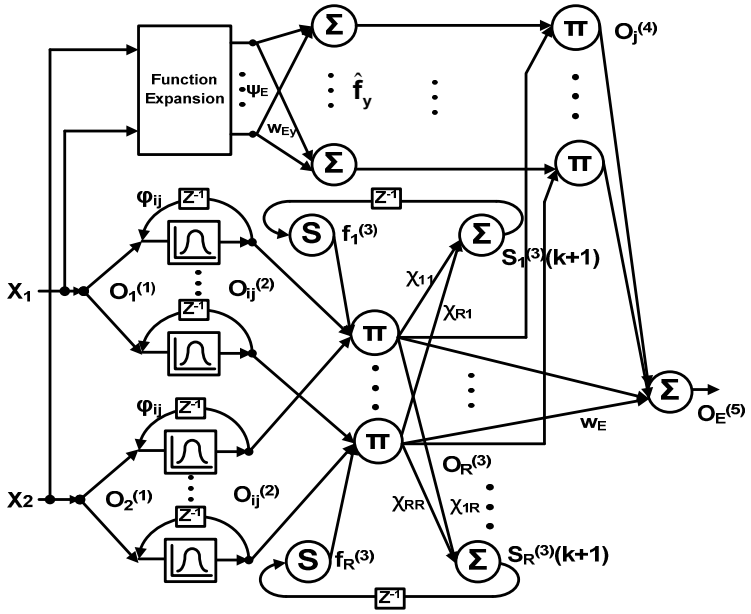

Figure 5. FLNRFNN structure.

The FLNRFNN input $\boldsymbol{X} = [\Delta\omega_{\mathrm{MS}}, \frac{d}{dt}(\Delta\omega_{\mathrm{MS}})]^{\mathrm{T}}$ is used by the power system to directly transmit the numerical inputs to the next layer in this study. Therefore, the FLNRFNN can employ the neurons to increase dynamic characteristics of the network. The novel RFNN (NRFNN) can retain dynamic characteristics of the network through trainings of the weights φ_{ij} and χ_{RR}, and has a better dynamic response than that of the general RFNN. The node output of each layer of the FLNRFNN and the superscripts present the layer-number of the output O, while the subscripts present the signal number of the related output, and these are given as follows:

$$O_i^{(1)}(t) = X_i^{(1)}(t)\ i = 1,\ 2 \tag{20}$$

$$O_{ij}^{(2)}(k) = exp\left\{ -\frac{\left(O_i^{(1)}(k) + O_{ij}^{(2)}(k-1)\cdot\varphi_{ij} - m_{ij}\right)^2}{(\sigma_{ij})^2} \right\} \tag{21}$$

$$f_R(k) = \frac{1}{1+\exp(-S_R)} \tag{22}$$

$$O_R^{(3)}(k) = f_R \cdot \prod_{i=1}^{2} O_{ij}^{(2)}(k)\cdot w_{ij} \tag{23}$$

$$O_j^{(4)}(k) = \prod O_R^{(3)}(k)\cdot\hat{f}_y(k) \tag{24}$$

$$O_{\mathrm{E}}^{(5)}(k) = \frac{\sum_{R=1}^{p} O_R^{(3)}(k)\hat{f}_y(k)}{\sum_{R=1}^{p} w_E O_R^{(3)}(k)} \tag{25}$$

where k denotes the iteration number of FLNRFNN. m_{ij} is the Mean, σ_{ij} is the Standard Deviation (STD) of the i-term input linguistic variable $O_i^{(1)}$ in the j-term. $R \in \{1,\ 2,\ 3\cdots, j\times j\}; w_E = w_{ij} = 1; \chi_{RR}$ is the recurrent weight. The parameters of the FLNRFNN to be trained are σ_{ij}, m_{ij}, w_{Ey}, φ_{ij} and χ_{RR}. $O_{\mathrm{E}}^{(5)}$ is called an output linguistic node. This performs the operation of defuzzification. The objective of the FLNRFNN controller is to train the parameters σ_{ij}, m_{ij}, w_{Ey}, φ_{ij} and χ_{RR} to make the best match with regard to the control signal.

3.3. Adaptive Critic Network

An adaptive critic network can be continuously trained forward in order to learn the cost-to-go function associated with the power system and produce the sensitivity of FLNRFNN. This ability is of great importance for real time optimal control operations when there are changes in configuration and operating conditions. The cost-to-go function J of Bellman's equation of dynamic programming estimated by the critic network is [21,22]:

$$J(t) = \sum_{k=0}^{\infty} \gamma^k U(t+k) = U(t) + \sum_{k=0}^{\infty} \gamma^k U[(t+1)+k] = U(t) + \gamma \cdot J(t+1) \tag{26}$$

where the $U(t)$ is an important effect to form the optimal cost-to-go function. The utility function of the critic network includes $U(t)$, as follows:

$$U(t) = |\Delta\omega_{\mathrm{MS}}(t) + \Delta\omega_{\mathrm{MS}}(t-1) + \Delta\omega_{\mathrm{MS}}(t-2)| \tag{27}$$

The node output of each layer of the critic network and the superscripts represent the layer-number of the output Oc, while the subscripts present the signal number of the related output, and these are given as:

$$Oc_i^{(1)}(t) = F_i^{(1)}(t),\ i = 1, \ldots, 7 \tag{28}$$

$$Oc_i^{(2)}(t) = \frac{1}{1 + exp^{H}},\ H = \sum_{i=1}^{8} Oc_i^{(1)} \cdot w_{ab} \tag{29}$$

$$Oc_n^{(3)}(t) = J_n(t) = \sum_{n=1}^{2} Oc_i^{(2)},\ n = 1, 2 \tag{30}$$

$$Oc^{(4)}(t) = \sum Oc_n^{(3)} = J(t) \tag{31}$$

where w_{ab} is the connecting weights of the input layer to the hidden layer. The node input of critic network F_i = [$\Delta\omega_{\mathrm{MS}}(t-1)$, $\Delta\omega_{\mathrm{MS}}(t-2)$, $\Delta K_P(t)$, $\Delta K_I(t)$, $\Delta K_D(t)$, 1].

Using Equation (27), the STATCOM should improve the performance of generator speed deviation $\Delta\omega_{\mathrm{MS}}$. The adaptive critic network in Figure 6 has a four-layer feed-forward network structure. The training process ensures that the critic network provides optimal control to minimize the $J(t)$, which enables the FLNRFNN controller to provide the optimal damping control signal to the STATCOM.

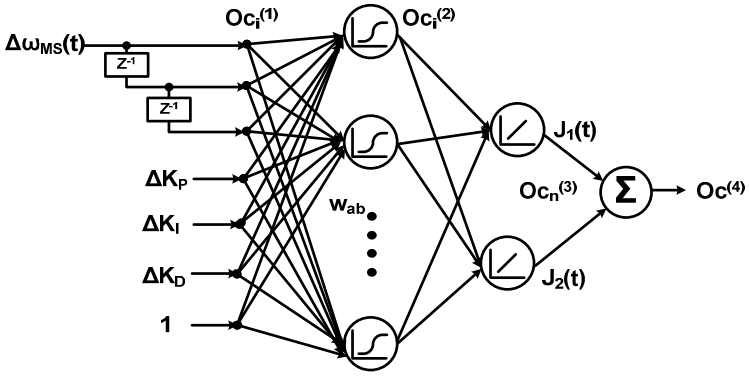

Figure 6. Critic network structure.

3.4. The Training Process of FLNRFNN and Critic Network

The gradient of the error function is the direction to which the function increases. Therefore, searching the opposite side of the gradient can force the cost-to-go function to be minimized.

The gradient descent algorithm with the mean squared error function as the error function E can be defined by [21,22]:

$$E = 0.5[J^*(t) - J(t)]^2 = 0.5[U(t) + \gamma \cdot J^*(t+1) - J(t)]^2 \quad (32)$$

where the $J^*(t)$ is zero in the case of dealing with deviation signals.

The error term in direct proportion to the amount that weight w_{ab} is modified, and can be used to produce the instantaneous estimates of the negative gradient. The critic network and proposed FLNRFNN, the gradient based on the chain rule of the error term can be represented as Equations (33)–(36) for an online supervised training algorithm. The formulae for adjusting the w_{ab} of the critic network and the weight $w_{FLNRFNN}$ of FLNRFNN [23,24].

$$\frac{\partial E}{\partial w_{ab}} = \frac{\partial E}{\partial J} \cdot \frac{\partial J}{\partial w_{ab}} \quad (33)$$

$$\frac{\partial E}{\partial W_{FLNRFNN}} = \frac{\partial E}{\partial J} \cdot \frac{\partial J}{\partial \Delta K_{PID}} \cdot \frac{\partial \Delta K_{PID}}{\partial W_{FLNRFNN}} \quad (34)$$

$$w_{ab}(t+1) = w_{ab}(t) - \eta_{ab} \cdot \frac{\partial E(t)}{w_{ab}(t)} \quad (35)$$

$$W_{FLNRFNN}(t+1) = W_{FLNRFNN}(t) - \eta_{FL} \cdot \frac{\partial E(t)}{W_{FLNRFNN}(t)} \quad (36)$$

where η_{ab} is the learning rate of w_{ab}. $W_{FLENN} = [w_{ij},\ w_{rj},\ w_{jy}, w_{Ey}]$, and $\eta_{FL} = [\eta_{ij},\ \eta_{rj},\ \eta_{jy}, \eta_{Ey}]$ are the learning rates of $W_{FLNRFNN}$. ΔK_{PID} = [ΔK_P, ΔK_I, ΔK_D]. The critic network produces the sensitivity of FLNRFNN $\frac{\partial J}{\partial \Delta K_{PID}}$ as:

$$\frac{\partial J}{\partial \Delta K_{PID}} = \frac{\partial J}{Oc^{(4)}} \cdot \frac{Oc^{(4)}}{Oc_n^{(3)}} \cdot \frac{Oc_n^{(3)}}{Oc_i^{(2)}(t)} \cdot \frac{Oc_i^{(2)}(t)}{\partial \Delta K_{PID}} \quad (37)$$

4. Case Studies and Simulation Results

Many simulation tests were carried out to test the damping enhancement capability of the NIDC used for the STATCOM with the hybrid power multi-system. The integration of the OWF and SWPF connected to a hybrid power multi-system [25] in Figure 1 is built in a Power System Computer Aided Design/Electromagnetic Transients including DC (PSCAD/EMTDC) environment. The FLNRFNN and critic network were implemented in a MATLAB 7.0 program module. The parameters and initial values of the system are shown in the Appendix A. The cases are described here to illustrate the proposed method under different operating conditions. In order to examine whether the effectiveness of the proposed NIDC (the SW_3 is closed in Figure 3) is better than other intelligent control systems, it is compared with the external linear damping controller (the SW_1 is closed and SW_2 is opened in Figure 2), only the designed PID controllers (the SW_3 is opened in Figure 3) and the Grey-Elman Neural Network (G-ENN) [12], with the parameters used in this work being taken from the reference.

The following cases for Figure 1 are used to demonstrate the proposed method. In these simulation cases, the DFIG-based OWF and the SCIG-based SWPF air velocity are assumed to be 12 m/s and 8 m/s.

Case 1: A three-line-to-ground fault (balanced fault) occurs on phases *a*, *b* and *c* of bus 4, and is simulated at the first second for a duration of 100 ms [26].

Case 2: A single-line-to-ground fault (imbalanced fault) occurs on phase *a* of bus 4, and is simulated at the first second for a duration of 100 ms.

Case 3: Dynamic responses for SWPF air velocity and OWF speed change at the first second to fourth second and the tenth second to twentieth second, respectively.

The real power variations during the fault of Case 1 are shown in Figure 7a,b. The STATCOM with the NIDC has a better damping effect and a faster convergence rate than the external linear damping controller, the designed PID damping controller and the G-ENN. The dynamic responses of

rotor speed of the DFIG and SCIG are shown in Figure 7c,d. The NIDC generators rotor speed of the DFIG-based OWF and the SCIG-based SWPF can recover more quickly to the steady state around 1.9 and 2.5 s. Figure 8a–d illustrates the rotor speeds of the MTG and SG, and the rotor angles δ_M and δ_S of the hybrid power multi-system. It can be found that the proposed method recovers more quickly to their corresponding steady states.

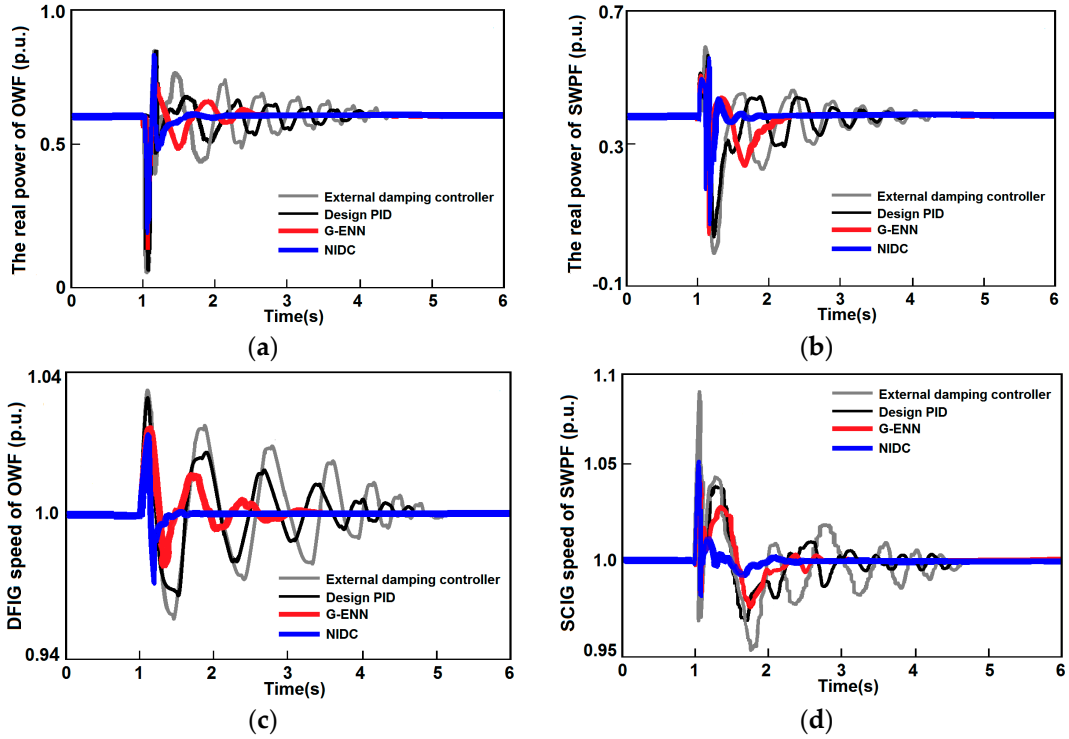

Figure 7. The responses of transient stability for OWF and SWPF in Case 1 (**a**) The real power of OWF; (**b**) The real power of SWPF; (**c**) The DFIG speed of OWF; (**d**) The SCIG speed of SWPF.

In Case 1, three-line-to-ground fault leads to large fluctuations in voltage at bus 4, thus maintaining that voltage stability is a high priority. Figure 9a shows that the STATCOM with the NIDC can effectively improve the voltage transient stability, and a faster voltage recovery is achieved to keep the bus voltage at 1.0 p.u. around 2 s. Figure 9b shows the STATCOM generates a small reactive power in order to maintain the bus voltage. The FLNRFNN to provide the variation PID parameters, ΔK_P, ΔK_I and ΔK_D are shown in Figure 9c. From Figure 9, it can be seen that the STATCOM with the proposed NIDC has a better transient stability for the hybrid multi-machine system.

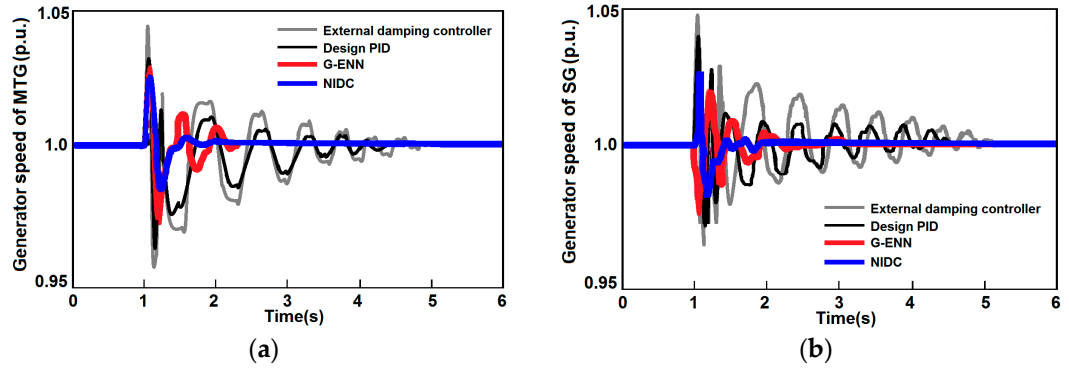

Figure 8. *Cont.*

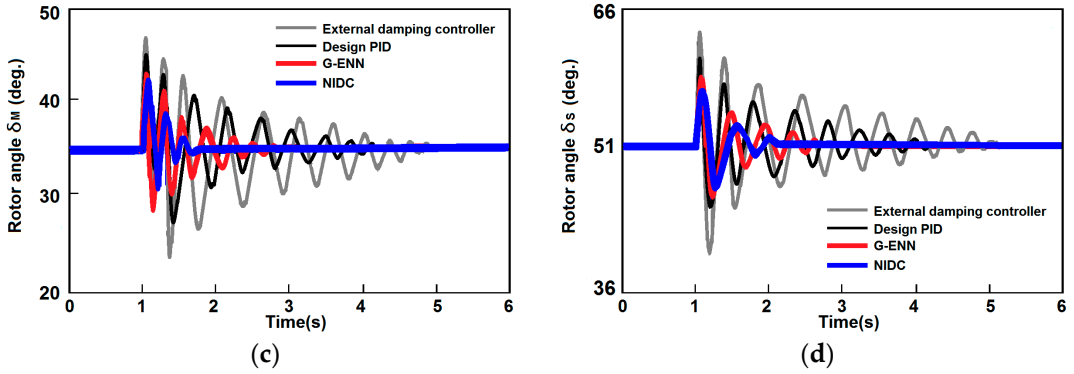

Figure 8. The responses of transient stability for the generators of hybrid power multi-system in Case 1 (**a**) The generator speed of MTG; (**b**) The generator speed of SG; (**c**) The rotor angle of MTG; (**d**) The rotor angle of SG.

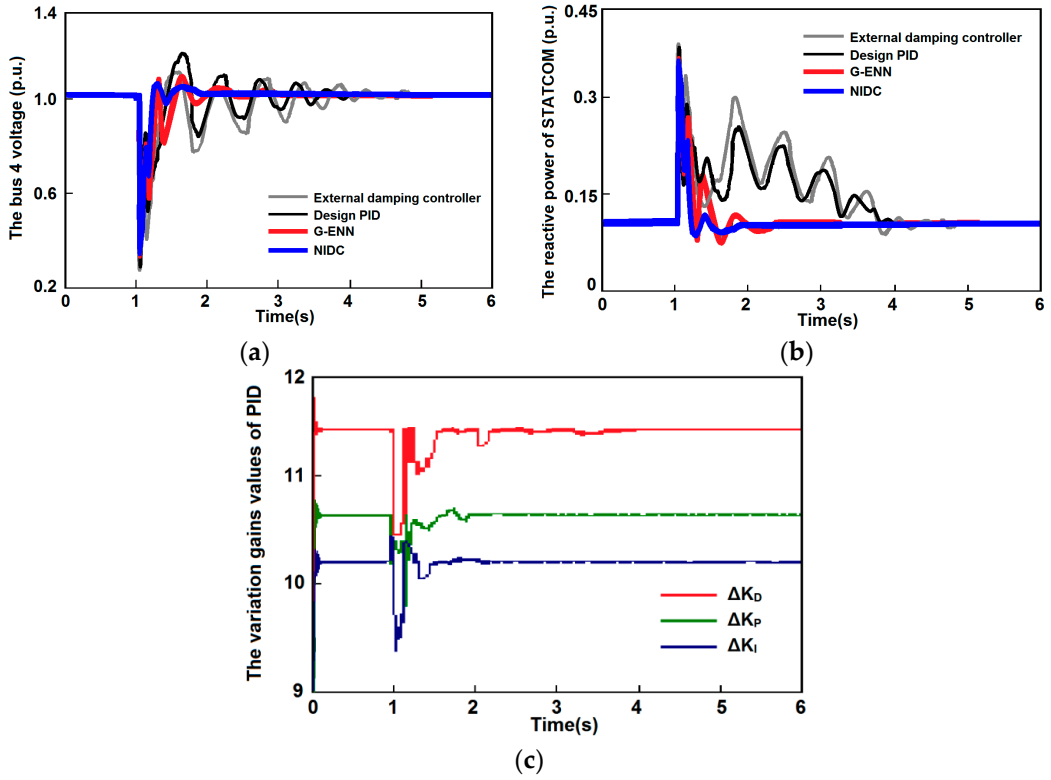

Figure 9. The responses of voltage, STATCOM and the variation PID parameters in Case 1 (**a**) The voltage of bus 4; (**b**) The reactive power of the STATCOM; (**c**) The variation PID parameters.

Figure 10 shows the transient responses during the fault of Case 2. Figure 10a,b shows the real power of the DFIG-based OWF and the SCIG-based SWPF connected to the multi-machine system. It can be seen that the STATCOM with the NIDC has a better damping effect and a faster convergence rate than the external linear damping controller, the designed PID damping controller and the G-ENN. From the Figure 10c, the STATCOM with the NIDC can effectively improve the voltage transient stability of bus 4, and a faster voltage recovery is achieved to keep the bus voltage at 1.0 p.u. around 1.6 s.

For Case 3, Figure 11a,b shows the real power variations during change. It illustrates the real power variations of the SWPF and OWF. The proposed NIDC can thus track faster and have more stable output power, leading to a better control. Figure 11c,d shows the dynamic responses of the

voltage magnitudes of bus 4. When the SWPF and OWF speed change, the proposed method has the smallest variations and a faster voltage recovery to keep the bus voltage at 1.0 p.u.

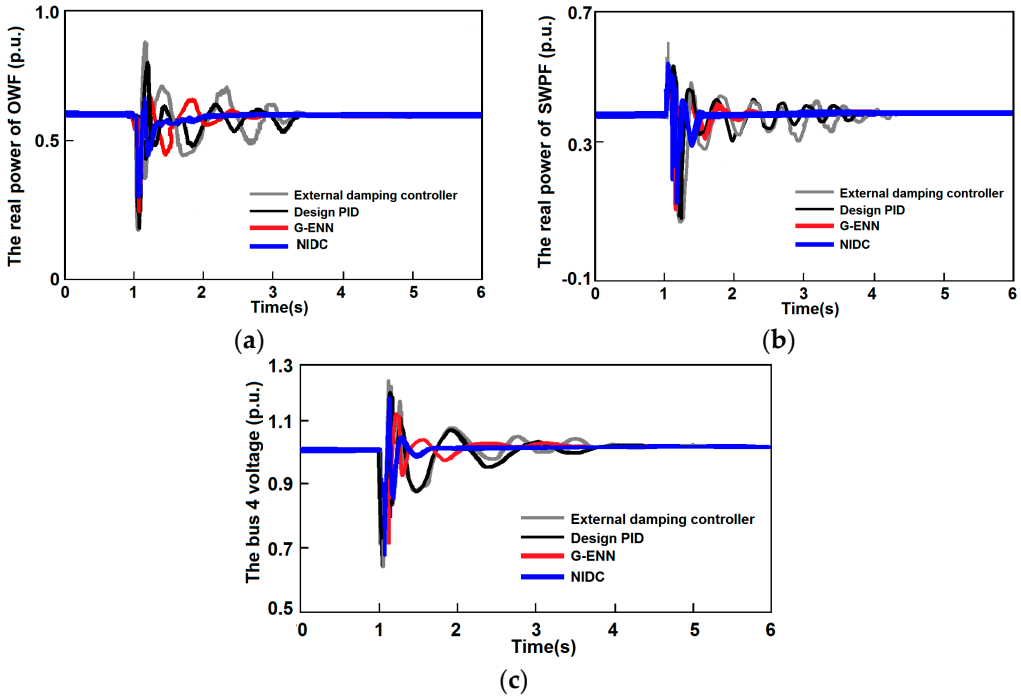

Figure 10. The responses of transient stability for Case 2 (**a**) The real power of OWF; (**b**) The real power of SWPF; (**c**) The voltage of bus 4.

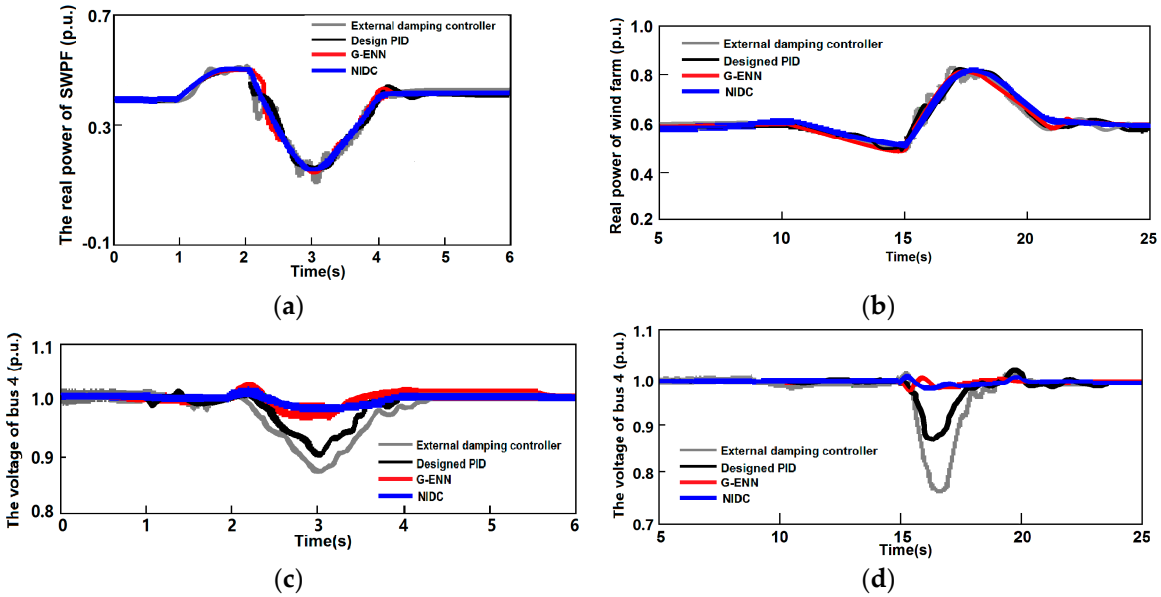

Figure 11. The responses of dynamic stability for Case 3 (**a**) The real power of SWPF; (**b**) The real power of OWF; (**c**) The voltage of bus 4 when SWPF air velocity changes; (**d**) The voltage of bus 4 when OWF speed changes.

5. Conclusions

An approach using NIDC for the STATCOM optimization is proposed in damping the oscillations of the power system integration of an OWF and an SWPF, linking to a hybrid power multi-system.

The transient responses of the studied system subjected to a balanced fault and an imbalanced fault demonstrate the effectiveness through simulation of the proposed method. Moreover, an efficient power sharing method among the hybrid energy sources was also presented, and the results show that this approach had greater efficiency, a better transient response and more stability than other approaches, even under different scenarios. The proposed NIDC for the STATCOM mitigates the oscillations and can also solve the problem of power stability. Reliability of scenario assessment becomes the major concern at this time. Further validation of this practical system will be reported in the near future.

Acknowledgments: The authors would like to thank anonymous reviewers for their valuable comments and insights. This research was partially supported by the Ministry of Science and Technology, Taiwan, R.O.C. under Grant no. MOST 104-3111-Y-042A-055.

Author Contributions: Ting-Chia Ou made substantial contributions to conception and plan; gave final approval of the version to be submitted. Kai-Hung Lu performed the experiments and conducted simulations; analysis and interpretation of data. Chiou-Jye Huang provided guidance.

Conflicts of Interest: The authors declare no conflict of interest.

Nomenclature

ρ	air density (kg/m^3)
A	disk radius of the rotor blades (m^2)
V_ω	wind velocity (m/s)
P_m	output mechanical power of wind turbine
C_p	power coefficient, and is given as a nonlinear function of the
λ	tip speed ratio
$\boldsymbol{\omega_r}$	turbine speed
β	blade pitch angle
$\boldsymbol{r}$	blade radius
ω_e	electrical angular frequency
T_m	mechanical torque
T_e	electrical torque
n_p	number of poles
J	inertia moment of WTG
B	friction coefficient of the generator
V	axial flow velocity
K	coefficient of Wells turbine
C_T	Wells turbine torque constant coefficients
$\mathrm{I_B}$	equivalent short-circuit current of BESS
$\mathrm{Z_B}$	series equivalent impedance of BESS
$\mathrm{V_{BESS}}$	terminal voltage of BESS
$\mathrm{X_{OWF}}$	state vector of the electric system of OWF
$\mathrm{X_{SWPF}}$	state vector of the electric system of SWPF
$\mathrm{X_{tur}}$	state vector of wind and Wells turbine systems
$\mathrm{X_{STATCOM}}$	state vector of STATCOM
V_S*	reference signal for the bus voltage
V_{dc}*	reference signals for dc link voltage
V_S	bus voltage
δ_S	phase angle of bus voltage
R_p	resistance of the STATCOM
i_{dcd}	d axis current values of STATCOM
i_{dcq}	q axis current values of STATCOM
ΔK_{PID}	variation gains values
$\hat{f}_y$	outer product term
w_{Ey}	connective weight

ψ_E	function expansion output
θ	basic functions
T_m	time constant of the washout filter
m_{ij}	Mean
σ_{ij}	Standard Deviation (STD)
E	error function
m	modulation index of PWM
α	phase shift of PWM
$\boldsymbol{\Delta\omega_{MS}}$	generator speed deviation
λ_1–λ_{21}	complex eigenvalues
ij	i-term input variable in the j-term
$J^*(t)$	reference value of the cost-to-go function
$U(t)$	utility function
γ	discount factor (0~1)

Appendix

The DFIG-based OWF:

$S = 10 \times 10$ MW, $V_R = 20$ KV, frequency = 50 Hz, $PF = 0.975$ lagging, $X_{TS} = X_{TR} =$ j0.08 p.u., $R_E = 0.02498\ \Omega$, $X_E = 0.0899$ mH, $X_C = 4387\ \mu$F, stator resistance = 0.006 p.u., stator inductance = 0.141 p.u., $C_F = 1840\ \mu$F, $\rho = 1.25$ kg/m^3, $r = 0.5$ m, $J = 1.32 \times 10^{-3}$ N·ms^2, $B = 5.78 \times 10^{-3}$ Nm·s/rad.

The SCIG-based SPWF:

$S = 6 \times 10$ MW, $K = 0.2$ $C_{T1} = C_{T2} = C_{T3} = 0.21$, $C_{T3} = C_{T4} = 0$, $C_{T5} = 0.1$, $C_{T6} = 6.14$, $C_{T7} = 13.2$, $C_{T8} = 0.0025$, $H = 0.5$, $D = 0.1$, stator resistance = 0.00488 p.u., stator inductance = 0.09955 p.u.

STATCOM with control system:

$S = 134$ MVA, Frequency = 50 Hz, $R_s = 0.04\ \Omega$, $L_s = 0.0001$ H, $K_{p1} = 0.31$, $K_{p2} = 0.25$, $K_{i1} = 0.15$, $K_{i2} = 0.12$.

NIDC: $\eta_{ij} = \eta_{rj} = \eta_{jy} = \eta_{Ey} = \eta_{ab} = 0.5$.

References

1. Waldner, M.; Erlich, I. Variable speed wind turbines based on electromechanical differential systems. *IEEE Trans. Energy Convers.* **2014**, *29*, 101–109. [CrossRef]
2. Cashman, D.P. Electrical Machine Characterisation and Analysis for Renewable Energy Applications. Ph.D. Thesis, University College Cork, Cork, Ireland, 2010.
3. Clément, A.; McCullen, P.; Falcão, A.; Fiorentino, A.; Gardner, F.; Hammarlund, K.; Lemonis, G.; Lewis, T.; Nielsen, K.; Petroncini, S.; et al. Wave energy utilisation in Europe: Current status and perspectives. *Renew. Sustain. Energy Rev.* **2002**, *6*, 405–431. [CrossRef]
4. Ou, T.C.; Tsao, T.P.; Lin, W.M.; Hong, C.M.; Lu, K.H.; Tu, C.S. A novel power flow analysis for microgrid distribution system. In Proceedings of the IEEE Conference on Industrial Electronics and Applications (ICIEA), Melbourne, Australia, 19–21 June 2013; pp. 1550–1555.
5. Ou, T.C.; Hong, C.M. Dynamic operation and control of microgrid hybrid power systems. *Energy* **2014**, *66*, 314–323. [CrossRef]
6. Ou, T.C. Ground fault current analysis with a direct building algorithm for microgrid distribution. *Int. J. Electr. Power Energy Syst.* **2013**, *53*, 867–875. [CrossRef]
7. Elsamahy, M.; Faried, S.O.; Sidhu, T. Voltage support control strategies for static synchronous compensators under unbalanced voltage sags. *IEEE Trans. Ind. Electron.* **2014**, *61*, 808–820.
8. Chen, W.L.; Liang, W.G.; Gau, H.S. Design of a mode decoupling STATCOM for voltage control of wind-driven induction generator systems. *IEEE Trans. Power Deliv.* **2010**, *25*, 1758–1767. [CrossRef]
9. Hong, C.M.; Ou, T.C.; Lu, K.H. Development of intelligent MPPT (maximum power point tracking) control for a grid-connected hybrid power generation system. *Energy* **2013**, *50*, 270–279. [CrossRef]
10. Fan, L.; Miao, Z. Mitigating SSR using DFIG-based wind generation. *IEEE Trans. Sustain. Energy* **2012**, *3*, 349–358. [CrossRef]
11. Hong, Y.Y.; Luo, Y.F. Optimal VAR control considering wind farms using probabilistic load-flow and gray-based genetic algorithms. *IEEE Trans. Power Deliv.* **2009**, *24*, 1441–1449. [CrossRef]
12. Mohagheghi, S.; Venayagamoorthy, G.K.; Harley, R.G. Optimal neuro-fuzzy external controller for a statcom in the 12-bus benchmark power system. *IEEE Trans. Power Deliv.* **2007**, *22*, 2548–2558. [CrossRef]

13. Lin, W.M.; Hong, C.M.; Huang, C.H.; Ou, T.C. Hybrid control of a wind induction generator based on grey–elman neural network. *IEEE Trans. Control Syst. Technol.* **2013**, *21*, 2367–2373. [CrossRef]
14. Lin, F.J.; Teng, L.T.; Lin, J.W.; Chen, S.Y. Recurrent functional link based fuzzy neural network controlled induction-generator system using improved particle swarm optimization. *IEEE Trans. Ind. Electron.* **2009**, *56*, 1557–1577.
15. Toh, K.A.; Yau, W.Y. Fingerprint and speaker verification decisions fusion using a functional link network. *IEEE Trans. Syst. Man Cybern. C* **2005**, *35*, 357–370. [CrossRef]
16. Lin, Y.Y.; Chang, J.Y.; Lin, C.T. Identification and prediction of dynamic systems using an interactively recurrent self-evolving fuzzy neural network. *IEEE Trans. Neural Netw. Learn. Syst.* **2012**, *24*, 310–321. [CrossRef] [PubMed]
17. Du, Y.; Wu, Q.; Jiang, C.; Wen, J. Adaptive functional link network control of near-space vehicles with dynamical uncertainties. *J. Syst. Eng. Electron.* **2012**, *21*, 868–876. [CrossRef]
18. Tang, Y.; Ju, P.; He, H.; Chuan, Q.; Feng, W. Optimized control of DFIG-based wind generation using sensitivity analysis and particle swarm optimization. *IEEE Trans. Smart Grid* **2013**, *4*, 509–520. [CrossRef]
19. Ou, T.C. A novel unsymmetrical faults analysis for microgrid distribution systems. *Int. J. Electr. Power Energy Syst.* **2012**, *43*, 1017–1024. [CrossRef]
20. Pai, F.S.; Huang, S.J. Design and operation of power converter for micro turbine powered distributed generator with capacity expansion capability. *IEEE Trans. Energy Convers.* **2008**, *21*, 110–118.
21. Ray, S.; Venayagamoorthy, G.K. Wide-area signal-based optimal neurocontroller for a UPFC. *IEEE Trans. Power Deliv.* **2008**, *2*, 1597–1605. [CrossRef]
22. Xu, X.; Hou, Z.; Lian, C. Online learning control using adaptive critic designs with sparse kernel machines. *IEEE Trans. Neural Netw. Learn. Syst.* **2013**, *24*, 762–775. [PubMed]
23. Farrag, M.E.A.; Putrus, G.A. Design of an adaptive neurofuzzy inference control system for the unified power-flow controller. *IEEE Trans. Power Deliv.* **2012**, *27*, 53–61. [CrossRef]
24. Lin, W.M.; Hong, C.M.; Ou, T.C.; Chiu, T.M. Hybrid intelligent control of PMSG wind generation system using pitch angle control with RBFN. *Energy Convers. Manag.* **2011**, *52*, 1244–1251. [CrossRef]
25. Mitra, P.; Venayagamoorthy, G.K.; Corzine, K.A. SmartPark as a virtual STATCOM. *IEEE Trans. Smart Grid* **2011**, *2*, 445–455. [CrossRef]
26. Lin, W.M.; Ou, T.C. Unbalanced distribution network fault analysis with hybrid compensation. *IET Gener. Transm. Distrib.* **2011**, *5*, 92–100. [CrossRef]